Applied Physics A (2025) 131:525
https://doi.org/10.1007/s00339-025-08643-3

Applied Physics A
Materials Science & Processing

Exploring the radiation attenuation potential on waste eggshell-derived SiO_2–CaO–B_2O_3–Na_2O–P_2O_5–CaF_2 bioactive glass for dental applications

Zhi Wei Loh[1] · Mohd Hafiz Mohd Zaid[1,2] · Khamirul Amin Matori[1,2] · Mohd Mustafa Awang Kechik[1] · Nor Kamilah Sa'at[1] · Izdihar Kamal[1] · Aishah Zarzali Shah[1,3] · Rosdiyana Hisam[4] · Wei Mun Cheong[5]

Received: 24 February 2025 / Accepted: 21 May 2025 / Published online: 2 June 2025

Abstract
This paper aims to study the radiation shielding potential of eggshell-derived bioactive glass with varying concentrations of calcium fluoride (CaF_2) using the Phy-X simulation. Attenuation parameters such as the linear attenuation coefficient (μ), mass attenuation coefficient (μ_m), half-value layer (HVL), mean free path (MFP), effective atomic number (Z_{eff}), exposure build-up factor (EBF), and energy absorption build-up factor (EABF) were evaluated across 0.015–15 MeV. The findings indicate that increasing CaF_2 content enhanced the μ_m and μ from 2.164 cm^2/g to 2.191 cm^2/g and 4.600 cm^{-1} to 4.671 cm^{-1} at the energy of 15 MeV. At 662 keV, the HVL and MFP ranged between 0.0398–0.0406 cm and 0.0574–0.0586 cm, outperforming conventional concrete and commercial glasses like RS 360 and RS 253 G18 by 98–99%. Furthermore, the Z_{eff} reaches a maximum of 15.463–16.046, while the EBF and EABF values drop with higher CaF_2 concentrations. These findings demonstrate the significant impact of CaF_2 addition in improving the mechanical and radiation attenuation features of bioactive glass. Consequently, the synthesized bioactive glass compositions show great promise as alternative attenuation materials for medical and industrial applications requiring effective ionizing radiation protection.

Keywords Bioactive glass · Radiation shielding · Phy-X · Attenuation · Mechanical

1 Introduction

Traditionally, biomaterials were developed to replace damaged tissues, with first-generation biomaterials specifically designed for their bio-inert properties to minimize scar tissue formation at the host tissues' interface. The discovery of bioactive glasses in the 1960 s marked a significant shift, introducing second-generation biomaterials capable of forming interfacial bonds with host tissues. This advancement led to third-generation biomaterials, such as Bioglass®, incorporating gene activation properties to enable tissue regeneration and repair. Since the discovery of 45S5 Bioglass® by Larry Hench [1], various chemical formulations have been reported to address research gaps. These bioactive glasses have been crucial in different applications, such as orthopaedics and dentistry. Bioactive glasses typically comprise SiO_2, CaO, Na_2O, and P_2O_5, with SiO_2 content between 35 wt.% and 50 wt.% for the melt-quenching method. Additional oxides, such as K_2O, TiO_2, and MgO, and various nanoparticles and fillers are incorporated to enhance specific properties [2–5]. Notably, adding CaF_2 to the bioactive glass not only brings advantages such as acid resistance and improved hardness but also has the potential to be used as radiation protection in the medical area [6].

Radiation has become a significant concern due to its widespread use in medical diagnostics, laboratories, and

✉ Mohd Hafiz Mohd Zaid
mhmzaid@upm.edu.my

1 Department of Physics, Faculty of Science, Universiti Putra Malaysia, UPM., 43400 Serdang, Selangor, Malaysia

2 Nanomaterials Synthesis and Characterization Laboratory, Institute of Nanoscience and Nanotechnology, Universiti Putra Malaysia, 43400 UPM Serdang, Selangor, Malaysia

3 Centre of Foundation Studies, Universiti Teknologi Mara, Cawangan Selangor, Kampus Dengkil, 43800 Dengkil, Selangor, Malaysia

4 Faculty of Applied Sciences, Universiti Teknologi MARA, 40450 Shah Alam, Selangor, Malaysia

5 Singapore Centre for 3D Printing, Nanyang Technological University, 50 Nanyang Avenue, Singapore 639798, Singapore

industrial applications, where high-energy sources emit X-rays, gamma rays, and neutrons [7]. Prolonged exposure to these rays can result in health issues such as radiation sickness and cancer, necessitating effective shielding materials. Conventional shielding materials like lead-based compounds and concrete are effective but face challenges related to cost, toxicity, and sustainability [8, 9]. In this context, glass emerges as a promising alternative due to its ease of manufacture, compositional versatility, and homogeneity [10, 11]. By tailoring their formulations with various oxides, glasses can be optimized for superior radiation attenuation [11–14].

Recent studies highlight the potential of bioactive glasses with specific additive oxides for enhanced radiation shielding. For instance, glasses with 15 mol.% ZnO achieved μ_m and μ values of 18.833 cm^2/g and 55.380 cm^{-1} at 0.015 MeV, demonstrating excellent radiation absorption and reduced shielding thickness requirements [15]. Similarly, the addition of SrO (0 to 6 wt.%) to bioactive glass increased the μ_m and Z_{eff}, highlighting its suitability for radiation attenuation [16]. Theoretical and simulation studies on fluoride-containing bioactive glasses showed µm improvements from 8.7469 cm^2/g to 11.1264 cm^2/g, confirming the positive role of fluoride in radiation shielding [17]. Further research on bioactive glass with TiO_2, aimed at applications in dental prosthetics and orthopaedic implants, found a 5 wt.% TiO_2 content resulted in optimal shielding features, with μ_m and HVL values of 7.304 cm^2/g and 0.030 cm, respectively, at 0.015 MeV [18]. Moreover, studies on silicate-based bioactive glasses with Gd_2O_3 addition showed improved attenuation qualities across a wide energy range. The HVL values decreased significantly, from 1.6712 cm to 0.9357 cm at 0.1 MeV, indicating enhanced shielding capability [19]. Another study reported on borate-based bioactive glass with WS_2 addition. The results showed that the μ_m values increased from 784.345 cm^2/g to 1180.868 cm^2/g with WS_2 up to 4 wt.%, alongside reduced build-up factors and improved photon attenuation efficiency [20]. Lastly, research on silicate-based bioactive glasses with varying B_2O_3 content found that samples without B_2O_3 content achieved the highest μ_m (3.781 cm^2/g) and μ (10.059 cm^{-1}) at 20 keV. These samples also exhibited HVL and mean free path (MFP) values of 0.030 cm and 0.044 cm at 15 keV, indicating superior radiation attenuation characteristics [21].

Despite their advantages in radiation shielding applications, bioactive glasses require further research and development to realize their full potential. While numerous studies have explored the fabrication, bioactivity, and biodegradability of bioactive glasses [22, 23], their radiation shielding capabilities remain underexplored and demand a deeper investigation. This research seeks to assess the radiation shielding potential of eggshell-derived bioactive glass using the Phy-X programme. Additionally, the study will examine the structural and mechanical characterization of the synthesized glasses to provide a comprehensive understanding of their performance. The outcomes of this research could offer significant insights into the advancement of bioactive glasses, facilitating their broader applications in medical and dental fields, necessitating efficient radiation protection.

2 Experimental procedure

2.1 Glass preparation

This work categorized the preparation into two parts. The first part is the extraction of calcium oxide from the waste eggshells. The waste eggshells were collected from the bakery in Bukit Serdang, Selangor, Malaysia and cleaned with deionized water. The cleaned eggshells were dried in an oven for 1 day to ensure they were completely dried before the next step. Then, the dried eggshells were crushed into pieces and placed in a square alumina boat for the calcination process. The eggshells were calcined at 900 °C for 120 min, and based on previous studies, this is the optimal temperature and duration for getting the highest purity of calcium oxide. The calcined eggshell powder was then ground and sieved for the mixing process. The second part is the preparation of pure chemicals, including Commercial SiO_2, Na_2CO_3 (Alfa Aesar, 99.5%), B_2O_3 (Acros Organics, 98%), P_2O_5 (Sigma-Aldrich), CaF_2 (R&M Chemicals, 97%), along with the prepared calcined eggshells (CaO) were weighted, ground homogenously and underwent melting and quenching process. Table 1 reveals the chemical formulation of each glass sample. The produced glass frits were prepared in powder form, and the sample powder was pressed into 13 mm pellet form.

2.2 Elemental and phase formation of eggshells

The raw eggshells and calcined eggshells were analyzed using an XRF instrument (ZSX Primus IV, Rigaku). The obtained results will show the intensity peaks versus energy graph, and the peak energy will identify the element with the purity in the samples. The phase formation of the raw eggshells and calcined eggshells was identified through an

Table 1 The chemical formulations of the glass

Glass code	Chemical composition
B1	$45SiO_2$–25Eggshells–$10B_2O_3$–10 Na_2O–$10P_2O_5$
B2	$45SiO_2$–25Eggshells–$10B_2O_3$–10 Na_2O–$8P_2O_5$–2 CaF_2
B3	$45SiO_2$–25Eggshells–$10B_2O_3$–10 Na_2O–$6P_2O_5$–4 CaF_2
B4	$45SiO_2$–25Eggshells–$10B_2O_3$–10 Na_2O–$4P_2O_5$–6 CaF_2
B5	$45SiO_2$–25Eggshells–$10B_2O_3$–10 Na_2O–$2P_2O_5$–8 CaF_2
B6	$45SiO_2$–25Eggshells–$10B_2O_3$–10 Na_2O–$8P_2O_5$–10 CaF_2

X-ray diffractometer with the model of PANalytical (Philips X' Pert Pro PW3050/60) with CuKα radiation λ = 1.5418 Å at 40 kV and 40 mA of the input current.

2.3 Thermal analysis

Differential Scanning Calorimetry (DSC) was conducted on the samples to identify the onset of glass transition temperature (T_g), crystallization onset temperature (T_x), crystallization peak temperature (T_c) and thermal stability factor (ΔT). The measurements were performed with a heating rate of 10 °C/min on a thermogravimetric analyzer (Mettler Toledo, TGA/DSC 1 HT) up to 900 °C, with each sample placed on a platinum crucible.

2.4 Structural and mechanical

The glass structure was identified through the diffractometer origin with model PW3050/60, with CuKα radiation (λ = 1.5418 Å), operated at 40 kV and 40 mA. Scans were performed over a 2θ range of 20° to 80° with a step size of 0.033° and a scan speed of 0.10°/min (equivalent to 19.685 s per step). The absorption spectra of the glass samples were analyzed to identify functional groups using a Fourier Transform Infrared (FTIR) spectrometer (Spectrum 100 Series, PerkinElmer) equipped with an Attenuated Total Reflectance (ATR) accessory, over the wavenumber range of 400–4000 cm^{-1}. The mechanical analysis, including microhardness and fracture toughness, was conducted on the samples through the Shimadzu micro-vickers model. The load used was 4.905 N for 15 s, while the fracture toughness was assessed using the Nihara formulation [22].

2.5 Radiation shielding measurement

Radiation protection is achieved by reducing the amount of radiation passing through the substance. Hence, the photon attenuation variables were calculated to assess the glass's radiation absorption across 0.015 to 15 MeV energy ranges. The computations were conducted utilizing the Phy-X/PSD programme, which enables simultaneous evaluation of multiple parameters, a notable advantage over other programs such as WinXcom which provides only one parameter [24]. The programme operates through three key steps. First, the materials' composition was defined, either in mole or weight fraction, coupled with the glass' density. Next, the ideal range of energy was specified, followed by selecting the relevant radiation shielding parameters. The MD-300S densimeter was used to assess each glass sample's density using Archimedes'principle, which can refer to the following references (Loh et al., 2023b, 2022; Shah et al., 2024).

In general, Beer-Lambert Law describes the photon attenuation properties of a material, providing a relationship between the material's thickness and the intensity of the gamma-ray beam. The following formula can be used to determine this relationship:

$$I = I_0 e^{-\mu x} \tag{1}$$

In this case, μ = linear attenuation coefficient, x = absorber thickness, and I_o and I = initial beam intensity and intensity of the gamma-ray after it has passed through the absorber. Then, the μ can be generated as shown:

$$\mu = \frac{1}{x}\ln\left(\frac{I_o}{I}\right) \tag{2}$$

The material's experimental, μ is estimated by the Beer-Lambert equation, but its attenuation features are greatly influenced by its density (ρ) [25]. Thus, for shielding calculations, the mass attenuation coefficient, $\mu_m = \mu/\rho$, is preferred and is determined by accounting for density (ρ) as shown:

$$\mu_m = \frac{1}{\rho x}\ln\left(\frac{I_o}{I}\right) \tag{3}$$

The μ_m is essential since it reflects materials' capacity to absorb radiation, which is affected by the incident photon energy and the glass density. Higher μ_m of material reveals a higher ability of protection [26]. Theoretically, the μ_m value can be generated from the programme and based on the additive "Mixture Rule", where the total μ_m of the component is the aggregate of the weight proportion of every single individual component inside the material.

$$\left(\mu_m\right)_{Total} = \sum_i w_i \left(\mu_m\right)_i \tag{4}$$

Meanwhile, the results from μ_m can be translated into other shielding data, for instance, half value layer (HVL), tenth value layer (TVL), mean free path (MFP), effective atomic number (Z_{eff}), and effective electron density (N_{eff}). For the sample to reduce the incoming radiation dosage by 50% and 10%, the thickness measurements HVL and TVL are required. Meanwhile, MFP is described as the average distance that a photon travels in a material before undergoing an interaction. These measurements could be calculated using the equations as shown:

$$HVL = \frac{\ln 2}{\mu} \tag{5}$$

$$TVL = \frac{\ln 10}{\mu} \tag{6}$$

$$TVL = \frac{\ln 10}{\mu} \tag{7}$$

The probability of photons interacting with atoms and electrons in a material at a specific energy value is described by the total atom cross-section (σ_a) and total electronic cross-section (σ_e). Both parameters could be computed through the formulations [27]:

$$\sigma_a = \frac{1}{N_A}\sum_i f_i A_i \left(\frac{\mu}{\rho}\right) i \tag{8}$$

$$\sigma_e = \frac{1}{N_A}\sum_j f_j \frac{A_j}{z_j}\left(\frac{\mu}{\rho}\right) j \tag{9}$$

Given that f_i and A_i = mole fraction and atomic weight of the i^{th} atomic element, respectively, Z_j = atomic number, and N_A = Avogadro constant. From here, the Z_{eff} varying energies are computed from the total atomic and electronic cross-section ratio using the formulation:

$$Z_{eff} = \frac{\sigma_a}{\sigma_e} \tag{10}$$

whereas N_{eff} = the quantity of electrons/unit mass of the shielding substance (expressed in electron/g) following the relation [28]:

$$N_{eff} = \frac{N_A}{A} Z_{eff} \tag{11}$$

Z_{eff} and N_{eff} are both crucial parameters for radiation shielding properties. The Z_{eff} varies with gamma-ray energy and represents a multi-element material in terms of an equivalent atomic number due to the different interactions and energy dependencies of gamma rays. Higher Z_{eff} materials are deemed to be excellent radiation absorbers because higher atomic number elements generally offer better radiation shielding. Meanwhile, N_{eff} shows how many electrons there are in each mass of material. Together, these parameters help understand how gamma rays interact with complex materials like glass for effective radiation shielding [29, 30]. Furthermore, the nuclear photon build-up factor (BF) must be meticulously considered while collecting nuclear data for purposes like radiation shielding and dose measurement. The BF is described to estimate and predict the photon flux distribution in the irradiated medium. There exist two BFs: the energy absorption buildup factor (EABF) and the exposure buildup factor (EBF). Several approaches have been used to calculate the BF values, with the Geometric Progression (G-P) fitting technique identified as the most appropriate and accurate [16, 20].

There are three steps to calculate the EBF.

The equivalent atomic number (Z_{eq}) must be determined first.
The G-P fitting parameters (b, c, a, X_k and d) are calculated in the second step.
Finally, figuring out the EBF is the third step.

The material's features are described by equivalent elements when the Z_{eq} of a glass made up of several elements matches the atomic number of a single element. One way to characterize the Z_{eq} is to estimate the proportion of the Compton partial μ_m to the total μ_m of a particular glass with a particular proportion of a single element at a particular energy. Thus, the Z_{eq} calculation can be obtained through the following formulation [31, 32]:

$$Z_{eq} = \frac{Z_1\left(\log R_2 - \log R\right) + Z_2\left(\log R - \log R_1\right)}{\log R_2 - \log R_1} \tag{12}$$

Given that Z_1 and Z_2 = element's atomic numbers correspond to the R_1 and R_2 ratios, where R = ratio of the specific glass at a certain energy. Next, the Z_{eq} values of the specific samples were subsequently chosen to compute the G-P fitting parameters (at 0.015 to 15 MeV), utilizing the formula as shown:

$$P = \frac{P_1\left(\log Z_2 - \log Z_{eq}\right) + P_2\left(\log Z_{eq} - \log Z_1\right)}{\log Z_2 - \log Z_1} \tag{13}$$

P_1 and P_2, corresponding to atomic numbers Z_1 and Z_2, are the G-P fitting parameters at a certain energy.

Lastly, the usage of the G-P fitting parameter to determine the EABF and EBF from 0.015 to 15 MeV, expanding to penetration depth 40 mfp, utilizing the equations as shown [33, 34]:

$$B(E,x) = 1 + \frac{b-1}{K-1}(K^x - 1); for K \neq 1 \tag{14}$$

$$B(E,x) = 1 + (b-1)x; for K = 1 \tag{15}$$

The photon dosage multiplication factor, or function K(E,x), could be computed through the formulation:

$$K(E,x) = cx^a + d\frac{\tanh\left(\frac{x}{X_k} - 2\right) - \tanh(-2)}{1 - \tanh(-2)}; \text{for} x \leq 40 \text{mfp} \tag{16}$$

Given that E = incident photon energy, x = source of the detector distance in the medium (unit = mfp), and b = BF at 1 mfp.

3 Results and discussion

3.1 Element and phase formation

The chemical composition of the calcined eggshells was analyzed using X-ray fluorescence (XRF) spectroscopy, as summarized in Table 2. The analysis revealed that CaO constituted the highest weight percentage at 97.90%. In addition to CaO, minor oxides such as MgO, Na_2O, Al_2O_3, SiO_2, P_2O_5, and K_2O, and others were also detected. These

findings are consistent with previous reports [35–37]. Furthermore, the decomposition of $CaCO_3$ into CaO with the release of CO_2 gas typically occurs between 600 °C and 850 °C [38, 39]. Based on various studies, calcination at 900 °C for 2 h is considered optimal to achieve the highest CaO yield with minimal impurities. Although minor oxides were present, their weight percentages were relatively low compared to the predominant CaO content. As such, their presence is not expected to significantly affect the glass composition. Nevertheless, these minor oxides can offer potential benefits to the glass system. SiO_2, Na_2O, and P_2O_5 are key components commonly utilized in bioactive glass fabrication. Meanwhile, MgO, Al_2O_3 and K_2O can enhance the biological and mechanical properties of the glass [40, 41]. However, it is important to note that excessive amounts of these oxides may reduce apatite formation, which could adversely affect the bioactivity of the glass [42] (Fig. 1).

Besides, the XRD patterns of uncalcined ($CaCO_3$) and calcined (CaO) eggshells are shown in Fig. 2. As shown in Fig. 2a, the uncalcined eggshells primarily consist of $CaCO_3$ in the calcite phase. Calcite, the most stable polymorph of $CaCO_3$ at room temperature and atmospheric pressure, is commonly found in eggshells and is suitable for biomedical and drug delivery applications [43]. Major diffraction peaks for calcite were observed at 2θ values of 29.62°, 39.61°, 43.46°, 47.41°, 48.77°, and 57.65°, matching ICSD No. 98–007–8882 and consistent with previous reports [38, 44]. Meanwhile, Fig. 2b presents the XRD results of eggshells calcined at 900 °C for 2 h. Calcination led to the transformation of $CaCO_3$ into CaO with a minor presence of $Ca(OH)_2$, attributed to moisture absorption during handling [45]. The major CaO diffraction peaks were detected at 2θ values of 32.42°, 37.56°, 54.06°, 64.35°, and 67.78° (ICSD No. 98–008–6048), while minor $Ca(OH)_2$ peaks appeared at 28.93°, 34.27°, 47.31°, and 51.04° (ICSD No. 98–005–7984). These findings are consistent with earlier

Table 2 XRF analysis of calcined eggshells

Composition	Weight percentage (wt.%)
CaO	97.9000
MgO	0.9030
Na_2O	0.1540
A_2O_3	0.1430
SiO_2	0.1400
P_2O_5	0.4040
SO_3	0.2200
K_2O	0.0436
Others	0.0924
Total	**100.0000**

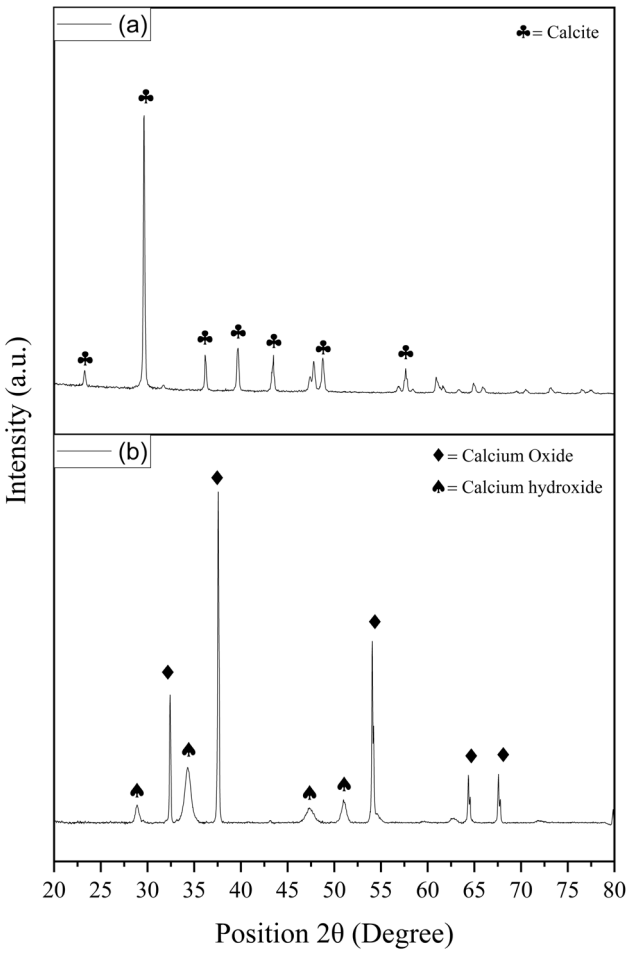

Fig. 1 XRD pattern of **a** uncalcined eggshells ($CaCO_3$) and **b** calcined eggshells (CaO)

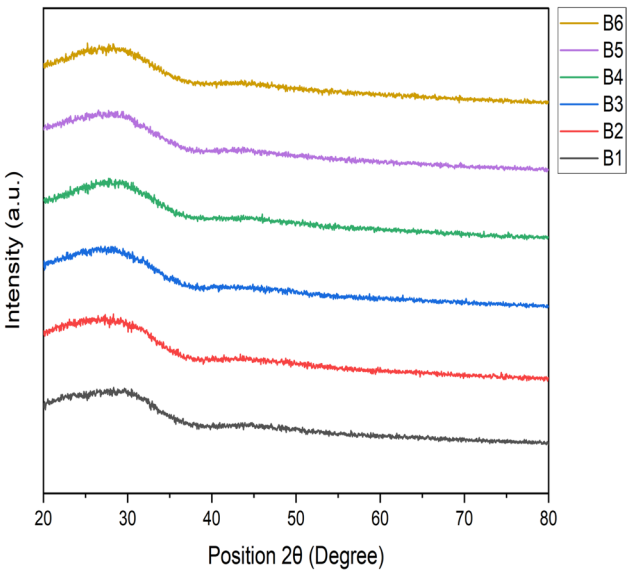

Fig. 2 XRD pattern of SiO_2–CaO–B_2O_3–Na_2O–P_2O_5–CaF_2 bioactive glasses

studies [35, 39]. Hence, calcination at 900 °C for 2 h produced high-quality crystalline CaO, confirming the critical role of temperature and duration in phase transformation.

3.2 Differential scanning calorimetry (DSC)

The DSC results of the glass samples are summarized in Table 3. All thermograms display a distinct onset of glass transition temperature (T_g), followed by the crystallization onset temperature (T_x) and crystallization peak temperature (T_c). The thermal stability (ΔT) was also evaluated. As shown in Table 3, T_g gradually decreased from 545 °C to 491 °C with increasing CaF_2 content. Similarly, T_c decreased from 682 °C to 652 °C as more CaF_2 was incorporated into the glass matrix. Interestingly, the thermal stability (ΔT) increased linearly from 108 °C to 141 °C (up to sample B4) before slightly decreasing to 138 °C with further CaF_2 addition. The presence of a distinct T_g followed by T_x and T_c, without any reported sharp melting point, further confirms the glassy nature of the samples.

3.3 X-ray diffraction (XRD) analysis

Figure 2 presents the XRD pattern of the glasses B1 to B6. The pattern shows a hump around $2\theta = 20°$ to 30° without the formation of any sharp peaks for all samples, indicating the amorphous nature of the glass. This amorphous structure arises from the random atomic arrangement in the glass, in contrast to the periodic, ordered atomic structure characteristic of crystalline materials. Based on previous studies, the addition of fluoride content of more than 10 wt.% to the glass will lead to early crystallization, affecting the bioactivity and biodegradability of the glass [46]. Therefore, the ideal range for fluoride addition to the glass system is less than 10 wt.%.

3.4 Fourier transform infrared (FTIR) analysis

Figure 3 presents the FTIR spectra graph of the glass samples, with the major vibrational modes assignments summarized in Table 4. The FTIR spectra revealed broad and overlapping bands rather than sharp, well-defined peaks, confirming the amorphous glassy nature of the glass samples. Characteristic Si–O–Si vibrations were detected around 440, 717, and 998 cm^{-1} corresponding to bending, stretching, and asymmetric stretching modes, respectively. These bands overlap with vibrational contributions from B–O–B ($[BO_3]$) and B–O ($[BO_4]$) units. A P–O bending mode near 552 cm^{-1} appeared in B1 to B4 and diminished with increasing CaF_2 content. Furthermore, the position of the Si–O–Si asymmetric stretching band around 998 cm^{-1} shifted to lower wavenumbers with increasing CaF_2. This shift is primarily attributed to the similar ionic radii of fluorine (1.36 Å) and oxygen (1.40 Å), which allows Si–F bonds to substitute for Si–O–Si linkages in the glass network. This substitution leads to a gradual disruption of the silica network, reduced structural stability, and the formation of non-bridging oxygen sites [47]. Based on these observations, fluoride primarily acts as a network modifier in the glass matrix. Additionally, the presence of a C–O stretching band around 1401 cm^{-1} is attributed to carbonate incorporation from CO_2 absorption during synthesis [48].

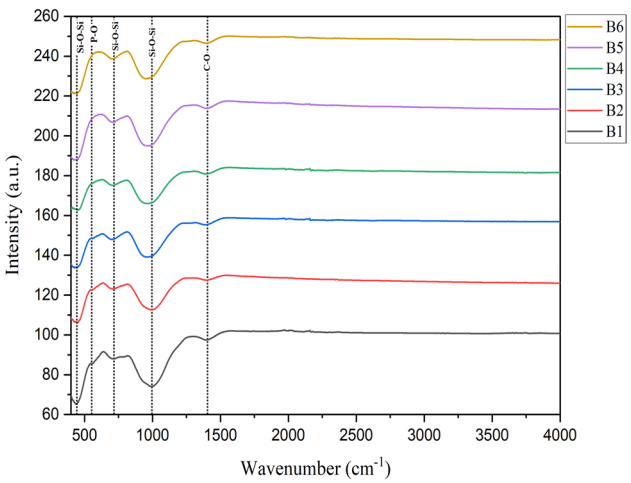

Fig. 3 FTIR spectra of the glass samples

Table 3 The DSC results of the glass samples

Glass	T_g(°C)	T_x(°C)	T_c(°C)	ΔT(°C)
B1	545	653	682	108
B2	519	650	677	131
B3	509	645	671	136
B4	496	637	662	141
B5	493	632	657	139
B6	491	629	652	138

Table 4 Band assignments of the glass samples

Wavenumber (cm^{-1})	Assignment of vibrational mode	References
~ 440	Si–O–Si bending mode	[49]
~ 552	P–O bending mode	[50]
~ 717	Si–O–Si stretching mode Si–O-B bending mode B–O–B stretching mode of $[BO_3]$	[51]
~ 956–998	Si–O–Si asymmetric stretching mode B–O stretching mode of $[BO_4]$	[52]
~ 1401	C–O stretching mode	[53]

3.5 Mechanical analysis

Vickers microhardness and fracture toughness are essential metrics for evaluating materials intended for orthopaedic and dental applications. Vickers microhardness measures a material's resistance to localized plastic deformation, providing insights into its durability and wear resistance under applied loads. Fracture toughness, on the other hand, evaluates the material's ability to resist crack propagation, ensuring its structural integrity under stress. Together, these measurements are crucial in determining whether a material possesses the necessary mechanical strength and reliability for specific biomedical applications, where performance and longevity are paramount.

Figure 4 presents the mechanical analysis of samples B1 to B6. The figure indicates an upward trend for Vickers microhardness from sample B1 to B4, ranging from 2.00 ± 0.07 GPa to 3.09 ± 0.07 GPa. In contrast, samples B5 and B6 show a slight decline, with values of 3.04 ± 0.06 GPa and 3.03 ± 0.03 GPa, respectively. Meanwhile, the fracture toughness shows a continuous increase from sample B1 with a value of 1.18 ± 0.04 MPa·$m^{1/2}$ to sample B6 with a value of 2.37 ± 0.09 MPa·$m^{1/2}$.

The initial increase in microhardness is attributed to enhanced glass compactness, as fluoride ions fill interstitial voids and promote the formation of bridging oxygen bonds, thereby strengthening the network. However, at higher fluoride concentrations, excessive network disruption results in the formation of non-bridging oxygen (NBO) sites and structural voids, reducing rigidity and leading to the observed decline in hardness. This disruption may also result in decreased grain size. Despite the reduction in hardness, fracture toughness continues to improve. The enhanced toughness at higher fluoride levels is explained by increased plastic deformation capacity and energy dissipation mechanisms, facilitated by the formation of strong ionic bonds and a more flexible glass network. These features enable the material to better resist crack propagation, even as its overall stiffness is reduced [54, 55].

3.6 Radiation shielding measurements

The range of energy used to analyze the radiation shielding findings of glasses was 0.01 MeV to 15 MeV. Generally, the photon can interact with matter through electromagnetic interaction due to three different mechanisms that mainly rely on the photon energy and the atomic number (*Z*), for instance, the Photoelectric effect (PE), Compton scattering (CS) and Pair production (PP) [18]. In PE, a single electron absorbs all the energy of an incident photon, while in CS, the incident photon transfers only a part of its energy to an electron. For PP, the photon energy can be utilized to produce an electron and positron pair if it is at least twice as great as the mass of an electron. Hence, considering the three energy ranges, the interactions are dominated by the PE in the energy range of less than 0.1 MeV and are based on the materials' atomic number, Z^{4-5}. Meanwhile, the CS process is linearly dependent on the *Z* of the materials and

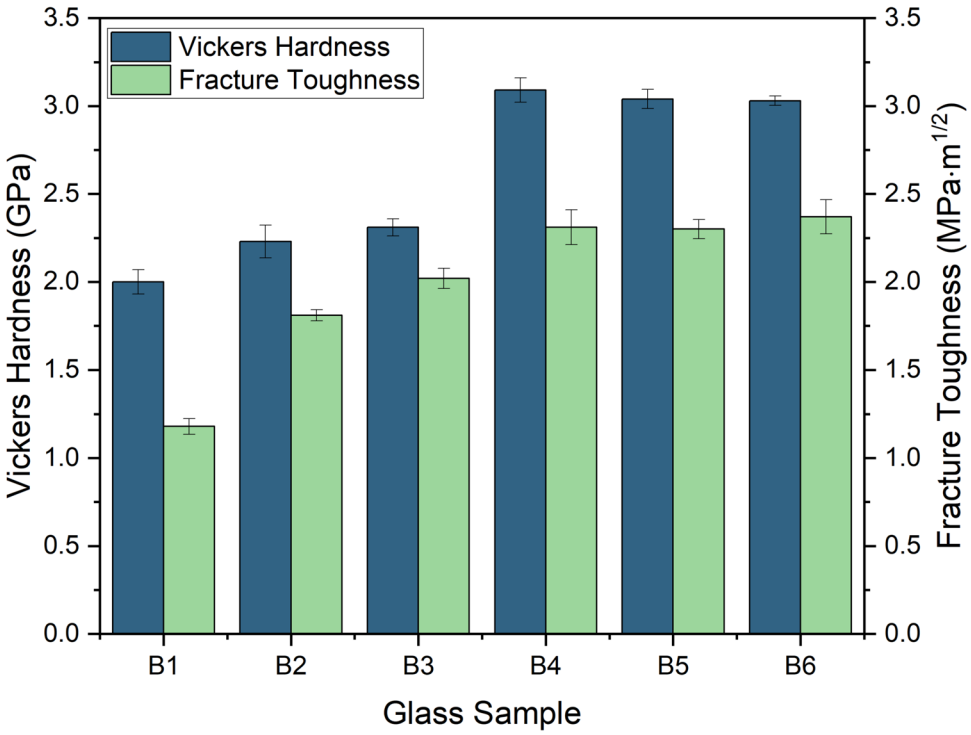

Fig. 4 Microhardness and toughness of SiO_2–CaO–B_2O_3–Na_2O–P_2O_5–CaF_2 bioactive glasses

dominates in the energy range of 0.1 MeV to 1 MeV. At energies above 1 MeV, the PP process dominates the interactions and is directly proportional to the Z^2.

Figure 5 reveals the μ_m of the glasses B1 to B6. It is apparent from the results that when the projectile energy escalates from 0.015 MeV to 15 MeV, the μ_m values of every sample progressively drop. This standard phenomenon occurs when a photon interacts with matter through the three interactions mentioned. Besides, as CaF_2 in the glass matrix rises from 0 wt.% to 10 wt.%, the μ_m data follow an ascending order. Each sample shows the maximum μ_m values located at 0.015 MeV and minimum μ_m values at 15 MeV. The highest μ_m values in the first region at 0.015 MeV are found in samples B1 through B6, which had respective values of 924.95 cm^2/g, 945.08 cm^2/g, 965.21 cm^2/g, 985.34 cm^2/g, 1005.47 cm^2/g and 1025.60 cm^2/g. The absorption of photons at low energy is mostly dominated by the PE. Then, each sample exhibited a fast drop in their μ_m values from 0.015 MeV up to 0.1 MeV, at which point the decrease slowed. The CS exhibits increased dominance in the second region with energy ranges of 0.1 MeV to 1 MeV. For instance, the μ_m of B1 drops from 924.95 cm^2/g to 2.16 cm^2/g, and in the case of B6, decreases from 1025.60 cm^2/g to 2.19 cm^2/g. Furthermore, as the energy increase from 1 MeV goes up to 15 MeV, the third region is dominated by the PP. As the photon energy increased, the μ_m readings began to steadily decline. Among the samples, B6 shows slightly higher μ_m values among the samples with the higher CaF_2 content. According to Alomayrah et al. (2024), glass with a higher percentage of high-Z elements will attenuate radiation more effectively [17]. Therefore, it can be claimed that the bioactive glass's attenuation coefficients were improved by the addition of CaF_2. A comparison of selected materials and their μ_m values at 0.015 MeV and 15 MeV is summarized in Table 5.

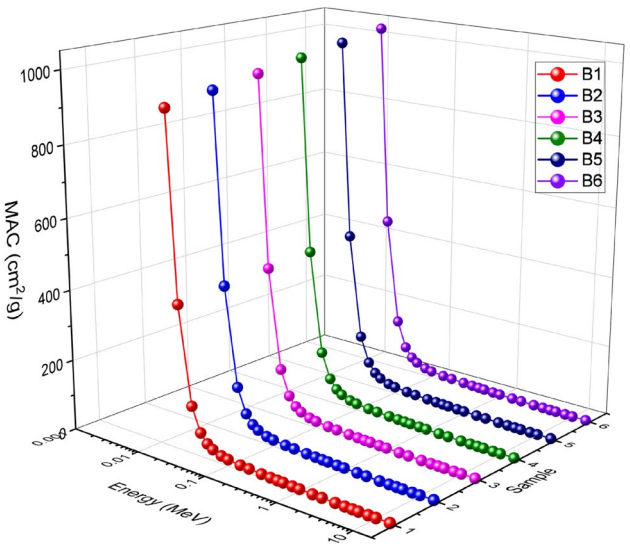

Fig. 5 μ_m against photon energy of SiO_2–CaO–B_2O_3–Na_2O–P_2O_5–CaF_2 bioactive glasses

Figure 6 illustrates the μ values for glasses B1 through B6. The graph illustrates that the μ changed with energy, mirroring the trend observed in the μ_m graph. The distinction between μ_m and μ is that μ considers the material's density, whereas μ_m does not. In this work, the samples exhibit an increase in density with rising CaF_2 concentration up to a specific threshold. In this case, the density of sample B1 rose from 2.126 g/cm^3 to 2.168 g/cm^3 for sample B4, and a drop in density was experienced at 2.132 g/cm^3 for sample B6. The reduced density for both B5 and B6 can be caused by the excessive CaF_2 that creates more non-bridging oxygen than bridging oxygen, resulting in a less dense silicate glass matrix [59]. The glass samples exhibit comparable behavior to that observed in μ_m, demonstrating significant radiation shielding capabilities against incoming photons in the lower energy region, primarily caused by the predominant PE interaction occurring within this range of energy. In the first region at 0.015 MeV, the μ values of samples B1 to B6 are 1966.45 cm^{-1}, 2018.69 cm^{-1}, 2071.34 cm^{-1}, 2136.22 cm^{-1}, 2144.67 cm^{-1}, and 2186.58 cm^{-1}. With the progression in photon energy, the μ values exhibit a sharp drop in the second region, specifically within the energy range of 0.1 MeV to 1 MeV, followed by a steady decline as energy rises from 1 to 15 MeV.

A crucial shielding characteristic for attenuator materials is the half-value layer (HVL), which denotes the thickness required to reduce the initial gamma-ray intensity by half. Figure 7 presents HVL against photon energy for the glasses B1 to B6. From the figure, The HVL values clearly increase with the rise in photon energy up to 15 MeV. At the onset of the lower energy spectrum, the required HVL is minimal, aligning with the restricted penetrating ability of the entering low-energy photons. In contrast, in the higher energy region, the thickness needed for the glasses increases, which is caused by the high penetrating characteristic of the incoming energy [60]. At 15 MeV, the HVL values are 0.1507 cm, 0.1496 cm, 0.1485 cm, 0.1467 cm, 0.1487 cm and 0.1484 cm for bioactive glasses B1 to B6, respectively, possessing an increasing order that with $(B4)_{HVL} < (B6)_{HVL} < (B3)_{HVL} < (B5)_{HVL} < (B2)_{HVL} < (B1)_{HVL}$. Among the samples, glass sample B3 with the optimal CaF_2 content achieved the lowest HVL with 0.1467 cm, reflecting that greater intensity of photons is obstructed at elevated CaF_2 content. Furthermore, Compton scattering is recognized as a pivotal mechanism in the energy absorption of soft tissue throughout the second and third energy ranges, specifically from 0.1 MeV to 10 MeV. Previous findings indicate that in a comparable energy range, the HVL of the silicate 13–93 bioactive glass samples was 1.6712 cm, which diminished to 0.9359 cm upon the incorporation of gadolinium into the

Table 5 A comparison of selected materials and their μ_m values at 0.015 MeV and 15 MeV

Materials	μ_m [0.015 MeV] (cm^2/g)	μ_m [15 MeV] (cm^2/g)	References
Lead-based glass (Ce-doped borate glass)	75	0.043	[56]
Lead silicate glasses	63.320–63.710	0.040–0.042	[57]
Ordinary concrete	7.7079	0.04881	[58]
Hematite-serpentine concrete	2.154	0.05955	[58]
Ilmenite-limonite concrete	2.964	0.07372	[58]
Basalt-magnetite concrete	2.047	0.07240	[58]
Ilmenite concrete	2.912	0.08803	[58]
Steel-scrap concrete	3.792	0.1089	[58]
Steel-magnetite concrete	4.511	0.1459	[58]
BaO-fluoride-phosphate glasses	0.147	0.0523	[24]
Fluoride-containing silicate glass (XCOM)	11.126	0.0222	[17]
Fluoride-containing silicate glass (FLUKA)	11.080	0.02213	[17]
WS_2-doped glass	784.345–1180.868	1.937–2.0275	[20]
Studied glass (this work)	924.95–1025.60	2.16–2.19	–

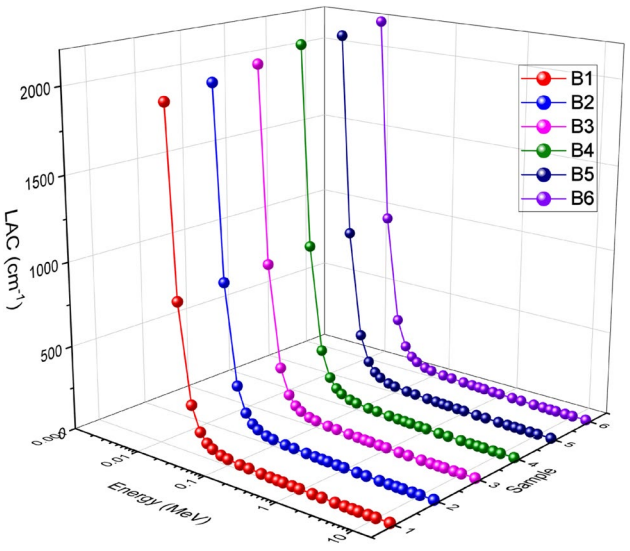

Fig. 6 μ against photon energy of SiO_2–CaO–B_2O_3–Na_2O–P_2O_5–CaF_2 bioactive glasses

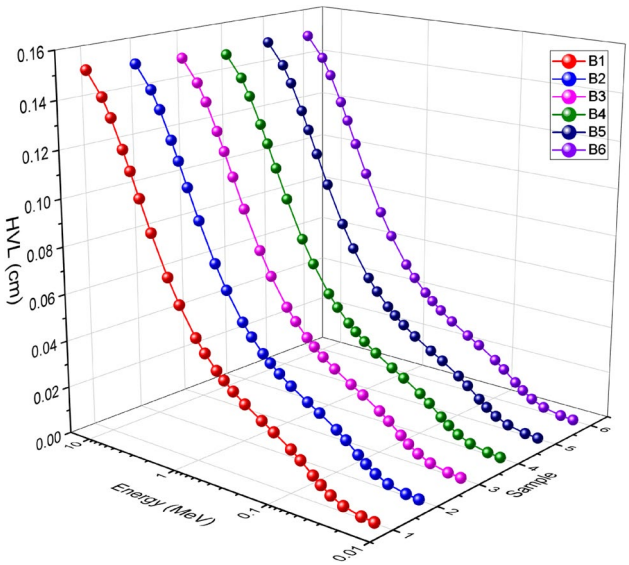

Fig. 7 HVL against photon energy of SiO_2–CaO–B_2O_3–Na_2O–P_2O_5–CaF_2 bioactive glasses

13–93 glass [19]. Yet, our glass sample B3 shows better results with the reduced need for the sample thickness of 0.0175 cm, which halves the incoming energy of 0.1 MeV. The comparison of the HVL values of our tested sample, together with the concrete and commercialize glasses used is shown in Table 6.

Furthermore, the photon shielding efficacy of glasses B1 to B6 is evaluated using the concept of the tenth value layer (TVL) as presented in Fig. 8. The TVL represents the attenuator's thickness required to reduce the intensity of gamma rays by a factor of 10. This characteristic is essential for the design of radiation protection glasses, used in X-ray windows and several medical field applications [24]. The TVL results display a trajectory akin to that of the HVL. The TVL rises with photon energy from 0.015 MeV to 15 MeV. However, it diminishes with higher CaF_2 concentration. Glass B4, with TVL of 0.4872 cm, attained the minimum thickness among the samples, hence enhancing its capacity to attenuate photons at 15 MeV.

Another important parameter in attenuation is the mean free path (MFP). MFP is interpreted as the distance required for radiation to interact with the substance before a second collision occurs. The reduced MFP distance will result in a smaller distance at the occurrence of the second radiation

Table 6 HVL and MFP of concretes, commercial glasses, and our tested bioactive glass system at the energy of ~0.662 MeV [60–62]

Shielding materials	HVL (cm)	MFP (cm)
Standard Concrete	3.880	-
Hematite Serpentitne Concrete	3.620	-
Ilmenite Limonite Concrete	3.190	-
Steel Reinforced Concrete	2.320	-
Commercial Window Glass	4.730	-
RS 253 & RS 253 G18	3.650	5.2616
RS 323 G18	2.480	3.5714
RS 360	2.170	3.125
RS 520	1.390	2.000
Tested Sample B4	0.0398	0.0575

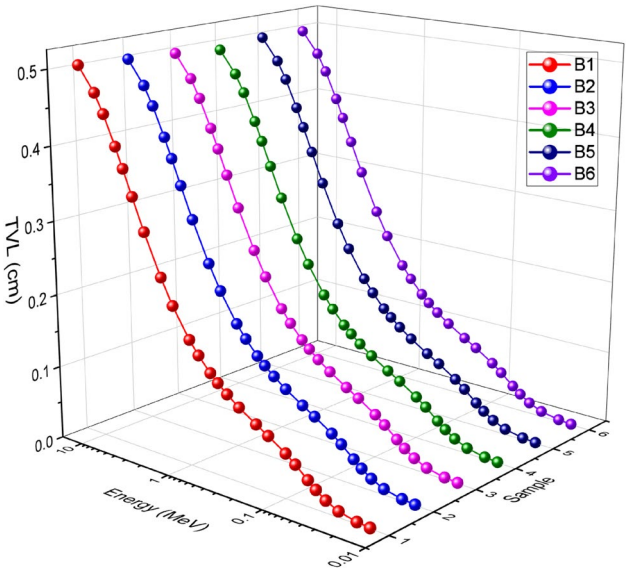

Fig. 8 TVL against photon energy of SiO_2–CaO–B_2O_3–Na_2O–P_2O_5–CaF_2 bioactive glasses

interaction [21]. Hence, the incoming photon energy will be absorbed by reducing it over short distances when the MFP is minimal. Hence, a smaller MFP of a material corresponds to a greater capacity for attenuation of the sample. MFP assists in ascertaining the requisite thickness and protection in dentistry and medical establishments. Figure 9 depicts the MFP in relation to the photon energy of glasses B1 through B6. A comparable tendency is evident in the HVL and TVL of the samples; the MFP escalates with the phonon energy up to 15 MeV. The MFP values for B1 to B6 are 0.2174 cm, 0.2158 cm, 0.2143 cm, 0.2116 cm, 0.2145 cm and 0.2141 cm, respectively. Higher density is associated with reduced MFP values, enabling the material to attenuate photons over shorter distances and decreasing the necessary glass thickness for effective shielding [61]. Among the

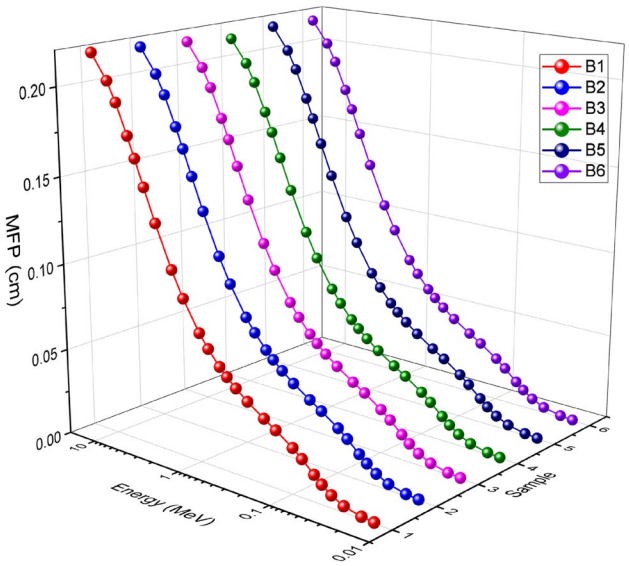

Fig. 9 MFP against photon energy of SiO_2–CaO–B_2O_3–Na_2O–P_2O_5–CaF_2 bioactive glasses

samples with varying CaF_2 concentrations, sample B4, with its higher density, achieved the lowest MFP value of 0.2116 cm, demonstrating superior radiation shielding properties. The MFP values for the commercial glasses and concrete utilized with our tested samples were compared and summarized in Table 6.

Generally, the effective atomic number (Z_{eff}) and the effective electron density (N_{eff}) are critical factors for characterizing photon interactions with materials. These parameters are vital for understanding gamma-ray

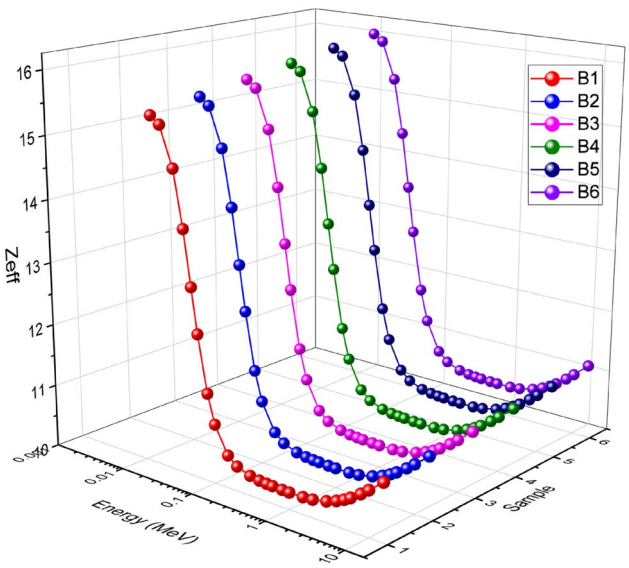

Fig. 10 Z_{eff} against photon energy of SiO_2–CaO–B_2O_3–Na_2O–P_2O_5–CaF_2 bioactive glasses

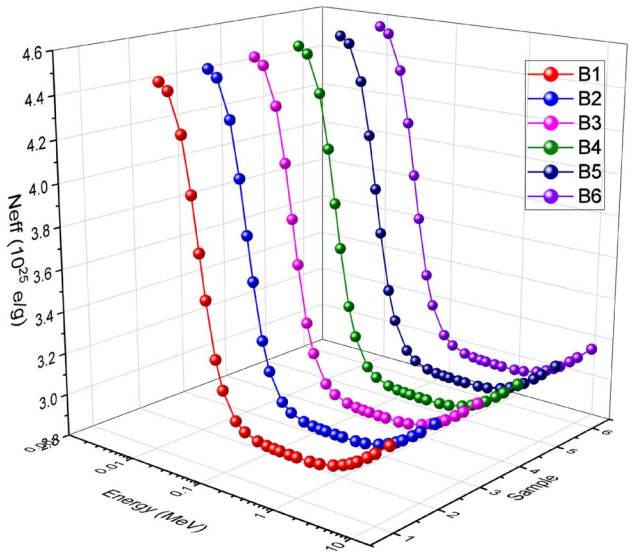

Fig. 11 N_{eff} against photon energy of SiO_2–CaO–B_2O_3–Na_2O–P_2O_5–CaF_2 bioactive glasses

interactions with complex materials like glass, which is crucial for effective radiation shielding (Shah et al., 2024). Figure 10 presents the Z_{eff} against photon energy for glasses B1 to B6. Higher Z_{eff} values correlate with enhanced shielding properties, reflecting the material's ability to obstruct incoming photons and minimize transmitted light [15]. From the figure, the maximum Z_{eff} values of all samples are found at 0.015 MeV and start to drop as photon energy increases to 1.5 MeV. The fluctuation in Z_{eff} is contributed by the predominance of distinct photon interaction processes through various energy ranges. In the low-energy zone (< 0.01 MeV), a sharp decline in Z_{eff} is attributed to the dominance of PE absorption. In the energy range of 0.01 MeV to 1.5 MeV, Z_{eff} stabilizes and is nearly independent of photon energy, as the interaction is primarily governed by CS. At energies above 1.5 MeV, PP becomes dominant, leading to a gradual increase in Z_{eff}, as revealed in Fig. 10. In addition, the presence of CaF_2 amplifies the increases in Z_{eff} owing to the elevated atomic number of the glass composition, with values progressively increasing to 15.46, 15.59, 15.71, 15.82, 15.94 and 16.05 for glasses B1 to B6, respectively. The trend observed in the N_{eff} graph aligns with that of Z_{eff}, with notably high N_{eff} values across all samples in the low-energy zone as presented in Fig. 11.

The nuclear photon BF must be considered while collecting nuclear figures for radiation shielding applications. The BF determines the target fraction supplied by the photons interacting with one other. The exposure buildup factor (EBF) and energy absorption buildup factor (EABF) against photon energy of B1 to B6 at varied mfp (0.5, 5, 10, 20

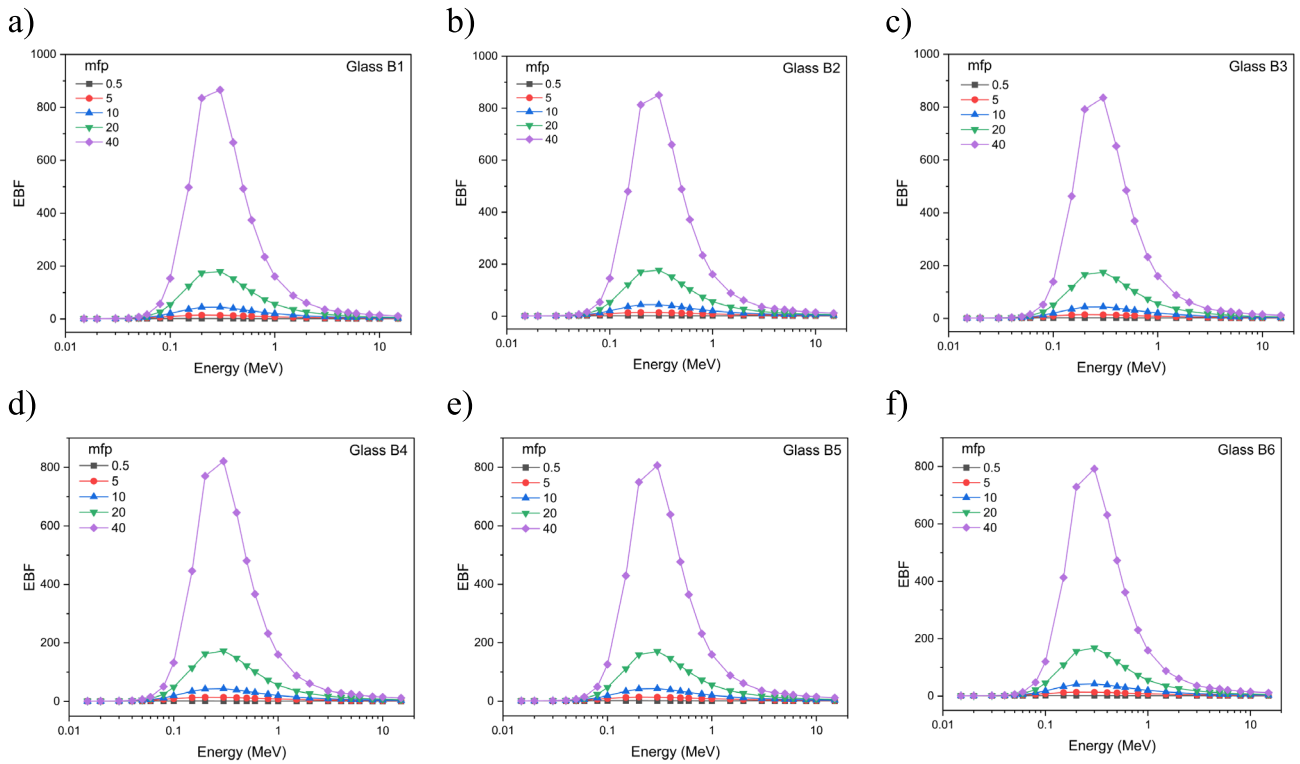

Fig. 12 EBF against photon energy of SiO_2–CaO–B_2O_3–Na_2O–P_2O_5–CaF_2 bioactive glasses

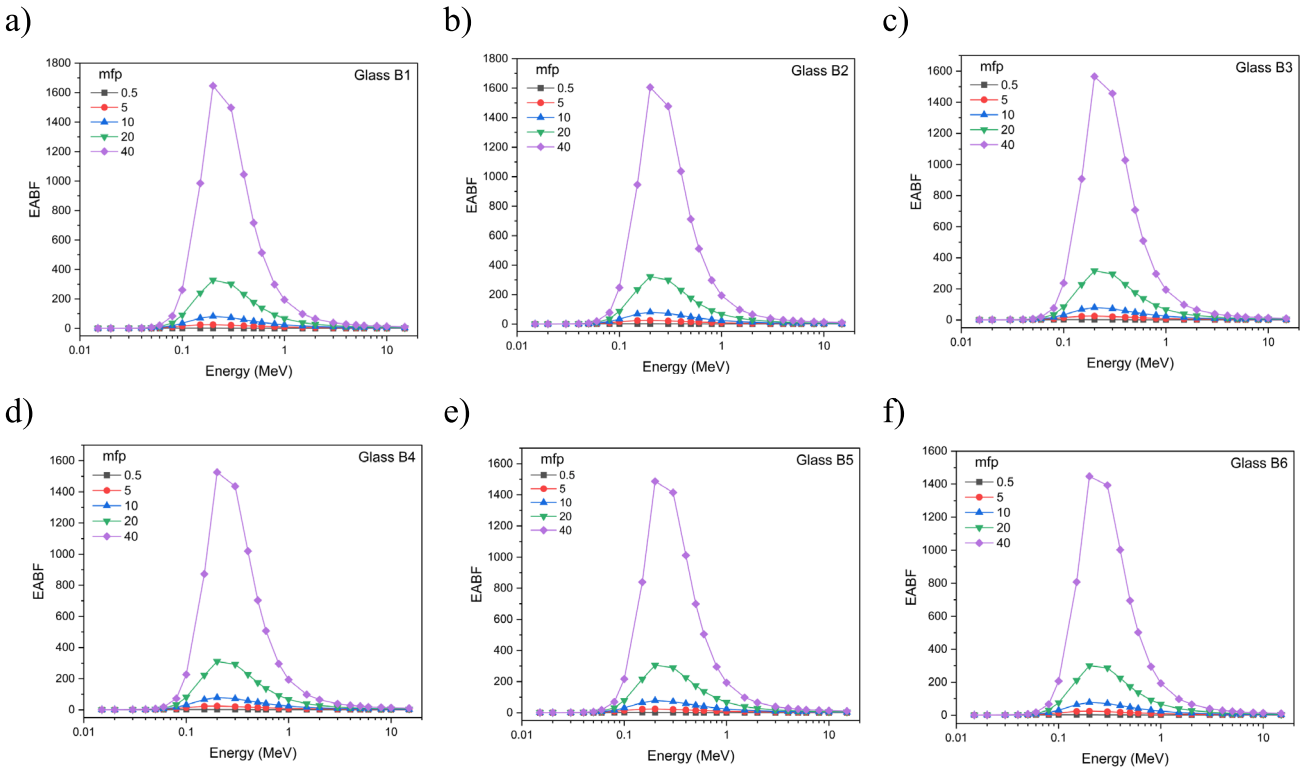

Fig. 13 EABF against photon energy of SiO_2–CaO–B_2O_3–Na_2O–P_2O_5–CaF_2 bioactive glasses

and 40) are presented in Figs. 12 and 13. According to the data, when the incident photon energy rises, the EBF and EABF data for all samples climb to a peak at intermediate energy before thereafter declining with a further increment of photon energy. This phenomenon can be comprehended by examining the prevalence of distinct photon interaction mechanisms through multiple energy domains [62]. In the low-energy domain, the PE interaction is the predominant process, resulting in substantial phonon absorption. Consequently, the values of EBF and EABF are diminished. Likewise, the PP takes over as the primary interaction process at higher energies. This mechanism also involves photon absorption but is more prevalent at elevated energy levels. Meanwhile, in the intermediate-energy region, CS dominates, causing photons to lose energy through scattering rather than being completely absorbed. This incomplete removal allows photons to persist longer within the material, increasing their likelihood of escaping [16, 34]. Consequently, this leads to higher EBF and EABF values. Hence, an effective shielding material should possess a high Z_{eff} value and a low BF. Both EBF and EABF values decrease with the CaF_2 concentration. Obviously, the inclusion of CaF_2 concentration in the bioactive glass will enhance the radiation shielding characteristics.

4 Conclusion

This study successfully synthesized eggshell-derived bioactive glasses with varied amounts of CaF_2 utilizing the melting and quenching process. The study concentrated on examining the structural, mechanical, and radiation shielding characteristics of the bioactive glass. All samples exhibited an amorphous structure, confirming their glassy nature, with no crystallization observed even with the addition of up to 10 wt.% CaF_2. In terms of mechanical, the addition of CaF_2 enhanced the hardness of the glasses, with values ranging from 2.00 ± 0.07 GPa to 3.09 ± 0.07 GPa. Radiation shielding characteristics, such as μ, μ_m, HVL, MFP, and Z_{eff}, were computed utilizing the Phy-X/PSD program for photon energies between 0.015 MeV and 15 MeV. The EBF and EABF were calculated with the G-P approach using photon energy corresponding to 40 mfp of penetration depths. The presence of CaF_2 markedly enhanced the radiation shielding characteristics of the glasses. Sample B4 demonstrated the least HVL and MFP values, whereas sample B6 exhibited the highest μ, μ_m, Z_{eff}, EBF, and EABF values, indicating superior shielding efficiency. Furthermore, all glass samples showed lower HVL and MFP values relative to traditional concrete and commercial glasses. The findings underscore

the prospective use of the synthesized bioactive glasses as alternative radiation shielding resources, rendering them appropriate for medical and industrial purposes that necessitate good protection against ionizing radiation.

Authors contribution Zhi Wei Loh: Formal Analysis, Investigation, Methodology, Software, Visualization, Writing – Original Draft. Mohd Hafiz Mohd Zaid: Conceptualization, Data curation, Funding acquisition, Project administration, Supervision, Validation, Writing – Original Draft. Khamirul Amin Matori: Data curation, Supervision, Validation, Writing – review & editing. Mohd Mustafa Awang Kechik: Software, Visualization, Writing – review & editing. Nor Kamilah Sa'at: Software, Visualization. Izdihar Kamal: Conceptualization, Resources. Aishah Zarzali Shah: Methodology, Visualization. Rosdiyana Hisam: Data curation, Validation, Wei Mun Cheong: Methodology, Software.

Funding This research was supported by Universiti Putra Malaysia via the Grant Putra Inisiatif (GPI/2023/9762700).

Data availability The data are available from the corresponding author on reasonable request.

Declarations

Ethics approval Not applicable.

Consent to participate Not applicable.

Consent for publication The authors consent to publish this article.

Competing interest The authors state that they have no recognized financial conflicts of interest or personal connections that could have impacted the research presented in this paper.

References

1. L.L. Hench, J. Mater. Sci. Mater. Med. **17**, 967 (2006)
2. A.M.A. Abdalla, Y.H. Elmoghazy, G.K. Sarkon, A. Gazioglu, O.K. Sabry, A.A. Sawelih, A. Al Sharif, H. Wehbi, A.Y. Ali Abd, S. Sahmani, and B. Safaei, Int. J. Adhes. Adhes. **138**, 103908 (2025)
3. J. Feng, B. Safaei, Z. Qin, F. Chu, F. Scarpa, Chem. Eng. J. **475**, 146382 (2023)
4. G. Ozankaya, M. Asmael, M. Alhijazi, B. Safaei, M. Y. Alibar, S. Arman, K. Kotrasova, V. Kvocak, M. Weissova, Q. Zeeshan, and D. Hui, Nanotechnol. Rev. **12**, (2023).
5. M. Asmael, Z. Al Mahmoud, S. Sahmani, and B. Safaei, Mater. Today Commun. **41**, 110854 (2024).
6. P.P. Sankaralingam, Indian J. Sci. Technol. **19**, 719 (2025)
7. J.S. Alzahrani, S. Alomairy, Z.A. Alrowaili, I.O. Olarinoye, C. Sriwunkum, M.S. Al-Buriahi, Radiat. Phys. Chem. **232**, 112688 (2025)
8. M.I. Sayyed, Silicon **16**, 1535 (2024)
9. U. Rilwan, G. M. Aliyu, S. F. Olukotun, M. M. Idris, A. A. Mundi, S. Bello, I. Umar, A. El-Taher, K. A. Mahmoud, and M. I. sayyed, Nucl. Eng. Technol. **56**, 2828 (2024).
10. M. Rezvani and H. Javid Ghezelgechi, Nucl. Eng. Technol. **57**, 103545 (2025).
11. E. Khalil, G. E. D. A. A. M, and R. M. R. Y. M. Moustafa, Opt. Quantum Electron. **57**, 1 (2025).
12. E.O. Ulas, A. Acikgoz, B. Aktas, Y. Kavun, Appl. Radiat. Isot. **221**, 111799 (2025)
13. N.S. Alsaiari, S.J. Alsufyani, Z.A. Alrowaili, C. Eke, C. Sriwunkum, M.S. Al-Buriahi, Radiat. Phys. Chem. **229**, 112500 (2025)
14. N. Khosravi, A. Moradi, F. Sharifianjazi, K. Tavamaishvili, A. Bakhtiari, J. Compos. Compunds **7**, 1 (2025)
15. H. Al-Ghamdi, N.A.M. Alsaif, A.A. El-Hamalawy, E.M. Ahmed, M.S. Sadeq, Y.S. Rammah, Radiat. Phys. Chem. **214**, 111278 (2024)
16. A.M.A. Mostafa, M.A.M. Uosif, Z.A. Alrowaili, S.A.M. Issa, V.Y. Ivanov, H.M. Zakaly, Radiat. Phys. Chem. **218**, 111641 (2024)
17. N. Alomayrah, M. M. Albarqi, R. A. Alsulami, Z. A. Alrowaili, C. Eke, I. Kebaili, I. O. Olarinoye, S. J. Alsufyani, and M. S. Al-Buriahi, Results Phys. **58**, (2024)
18. K. S. Shaaban, B. M. Alotaibi, N. Alharbi, Z. A. Alrowaili, M. S. Al-Buriahi, S. A. Makhlouf, and A. F. Abd El-Rehim, Radiat. Phys. Chem. **193**, 109995 (2022)
19. A. M. Deliormanlı, M. Ensoylu, S. A. M. Issa, Y. S. Rammah, G. ALMisned, and H. O. Tekin, Appl. Phys. A **128**, (2022)
20. A.M. Deliormanlı, M. Ensoylu, S.A.M. Issa, W. Elshami, A.M. Al-Baradi, M.S. Al-Buriahi, H.O. Tekin, Ceram. Int. **47**, 29739 (2021)
21. N. Al-Harbi, Y. Al-Hadeethi, A.S. Bakry, J. Non Cryst. Solids **552**, 120489 (2021)
22. Z. W. Loh, M. H. Mohd Zaid, M. M. Awang Kechik, Y. W. Fen, K. M. Amin, and W. M. Cheong, J. Mater. Res. Technol. **24**, 3815 (2023)
23. Z.W. Loh, M.H.M. Zaid, M.M.A. Kechik, Y.W. Fen, W.M. Cheong, M.Z.H. Mayzan, Mater. Lett. **361**, 136161 (2024)
24. Y. Al-Hadeethi, M.I. Sayyed, Prog. Nucl. Energy **126**, 103397 (2020)
25. A.S. Abouhaswa, M.I. Sayyed, A.S. Altowyan, Y. Al-Hadeethi, K.A. Mahmoud, J. Non Cryst. Solids **543**, 120134 (2020)
26. M. Alhassan, J. Baraya, A. Garba, J. Appl. Sceince Environ. Manag. **27**, 985 (2023)
27. K. I. Hussein, Int. J. Opt. Photonic Eng. **6**, (2021)
28. O. Agar, Cumhur. Sci. J. **39**, 983 (2018)
29. N. Karpuz, Int. J. Comput. Exp. Sci. Eng. **10**, 236 (2024)
30. B. Alim, Iğdır Üniversitesi Fen Bilim. Enstitüsü Derg. **10**, 202 (2020)
31. V.P. Singh, N.M. Badiger, Radiat. Phys. Chem. **104**, 61 (2014)
32. G. Lakshminarayana, S.O. Baki, K.M. Kaky, M.I. Sayyed, H.O. Tekin, A. Lira, I.V. Kityk, M.A. Mahdi, J. Non Cryst. Solids **471**, 222 (2017)
33. M.I. Sayyed, J. Alloys Compd. **695**, 3191 (2017)
34. M.I. Sayyed, H. Elhouichet, Radiat. Phys. Chem. **130**, 335 (2017)
35. N.H. Jakfar, S.F. Khor, B. Johar, N.M.S. Adzali, S.N.H.M. Yunus, E.M. Cheng, Int. J. Nanoelectron. Mater. **16**, 63 (2023)
36. S. Palakurthy, K.V. Reddy, S. Patel, P.A. Azeem, Prog. Biomater. **9**, 239 (2020)
37. A.A. Ayodeji, M.E. Ojewumi, B. Rasheed, J.M. Ayodele, Data Br. **19**, 1466 (2018)
38. M.I. Najah, I. Journal, M.I. Najah, A. Razak, N. Aida, C. Shukur, S. Adzila, R. Othman, N. Nordin, Int. J. Emerg. Trends Eng. Res. **8**, 6725 (2020)
39. N. Razali, N. Jumadi, A. Y. Jalani, N. Z. Kamarulzaman, and K. F. Pa'ee, Malaysian J. Anal. Sci. **26**, 347 (2022)
40. B. Karakuzu-İkizler, P. Terzioğlu, B.S. Oduncu-Tekerek, S. Yücel, J. Aust. Ceram. Soc. **56**, 697 (2020)
41. M. Ebrahimi, S. Manafi, F. Sharifianjazi, J. Non Cryst. Solids **606**, 122189 (2023)
42. A. Al-Noaman, S.C.F. Rawlinson, R.G. Hill, J. Non Cryst. Solids **358**, 1850 (2012)

43. M.H. Azarian, W. Sutapun, RSC Adv. **12**, 14729 (2022)
44. O.A.A. Eletta, O.A. Ajayi, O.O. Ogunleye, I.C. Akpan, J. Environ. Chem. Eng. **4**, 1367 (2016)
45. O. Awogbemi, F. Inambao, E.I. Onuh, Heliyon **6**, e05283 (2020)
46. R.A. Jalil, K.A. Matori, M.H.M. Zaid, N. Zainuddin, M.Z.A. Khiri, N.A.A. Rahman, W.N.W. Jusoh, E. Kul, J. Spectrosc. **2020**, 1 (2020)
47. F.A. Shah, Mater. Sci. Eng. C **58**, 1279 (2016)
48. N.F.B. Pallan, K.A. Matori, M. Hashim, R.S. Azis, N. Zainuddin, N.F.B. Pallan, F.M. Idris, I.R. Ibrahim, L.C. Wah, S.N.A. Rusly, N. Adnin, M.Z.A. Khiri, Z.N. Alassan, N. Mohamed, M.H.M. Zaid, Sci. Sinter. **51**, 377 (2019)
49. L. de Siqueira, T.M.B. Campos, S.E.A. Camargo, G.P. Thim, E.S. Trichês, J. Non Cryst. Solids **555**, 120629 (2021)
50. D. Kaur, M.S. Reddy, O.P. Pandey, J. Drug Deliv. Sci. Technol. **61**, 102154 (2020)
51. B. Karakuzu-Ikizler, P. Terzioğlu, Y. Basaran-Elalmis, B.S. Tekerek, S. Yücel, Bioact. Mater. **5**, 66 (2020)
52. R.M. Rad, A.Z. Alshemary, Z. Evis, D. Keskin, K. Altunbaş, A. Tezcaner, Ceram. Int. **44**, 13453 (2018)
53. V. Uskoković, G. Abuna, P. Ferreira, V.M. Wu, L. Gower, F.C.P. Pires-de-Souza, R.M. Murata, M.A.C. Sinhoreti, S. Geraldeli, J. Sol-Gel Sci. Technol. **97**, 245 (2021)
54. H.W. Kim, Y.J. Noh, Y.H. Koh, H.E. Kim, H.M. Kim, Biomaterials **23**, 4113 (2002)
55. A. Bachar, C. Mercier, A. Tricoteaux, S. Hampshire, A. Leriche, C. Follet, J. Mech. Behav. Biomed. Mater. **23**, 133 (2013)
56. E.M.A. Hussein, A.M. Madbouly, J. Aust. Ceram. Soc. **60**, 127 (2024)
57. Z. A. Alrowaili, N. Alomayrah, H. H. Saleh, C. Sriwunkum, A. Alalawi, and M. S. Al-Buriahi, Eur. Phys. J. Plus **140**, (2025)
58. I.I. Bashter, Ann. Nucl. Energy **24**, 1389 (1997)
59. A. Z. Shah, M. H. Mohd Zaid, K. A. Matori, Y. Yaakob, A. R. Sarmani, and R. Hisam, Prog. Nucl. Energy **171**, 105191 (2024)
60. G. Hoşgör, E. Tabar, Phys. Scr. **100**, 015308 (2025)
61. R. Kurtulus, T. Kavas, Cumhur. Sci. J. **41**, 976 (2020)
62. M.S. Al-Buriahi, I.O. Olarinoye, E. Yılmaz, F. Çalıskan, C. Sriwunkum, Ann. Nucl. Energy **213**, 111136 (2025)